

1 **This article is a preprint published at EarthArXiv**

2 **Notice - From the AMS Copyright Policy section 7c:**

3 This work is under review at the Journal of Climate. Copyright in this work may be
4 transferred without further notice. This work has not yet been peer-reviewed and is pro-
5 vided by the contributing author(s) as a means to ensure timely dissemination of schol-
6 arly and technical work on a noncommercial basis. Copyright and all rights therein are
7 maintained by the author(s) or by other copyright owners. It is understood that all per-
8 sons copying this information will adhere to the terms and constraints invoked by each au-
9 thor's copyright. This work may not be reposted without explicit permission of the copy-
10 right owner. [https://www.ametsoc.org/index.cfm/ams/publications/ethicalguidelines- and-ams-](https://www.ametsoc.org/index.cfm/ams/publications/ethicalguidelines-and-ams-policies/ams-copyright-policy)
11 [policies/ams-copyright-policy](https://www.ametsoc.org/index.cfm/ams/publications/ethicalguidelines-and-ams-policies/ams-copyright-policy).

12 **Supplemental Information for “Terrestrial evaporation and global climate:
13 lessons from Northland, a planet with a hemispheric continent”**

14 Marysa M. Laguë*

15 *Department of Earth and Planetary Science, University of California Berkeley, Berkeley, CA,*
16 *USA, and University of Saskatchewan Coldwater Lab, Canmore, Alberta, Canada*

17 Marianne Pietschnig

18 *Department of Mathematics, University of Exeter, Exeter, United Kingdom*

19 Sarah Ragen

20 *School of Oceanography, University of Washington, Seattle, WA, USA*

21 Timothy A. Smith

22 *Oden Institute for Computational Sciences, The University of Texas at Austin, Austin, TX, USA*

23 David S. Battisti

24 *Department of Atmospheric Sciences, University of Washington, Seattle, WA, USA*

25 **Corresponding author address: Marysa M. Laguë, Department of Earth and Planetary Science,*

26 *University of California Berkeley, 307 McCone Hall, Berkeley, CA 94720.*

27 *E-mail: mlague@berkeley.edu*

ABSTRACT

28

29 1. Hemispheric energy imbalance and the location of the Zonal mean ITCZ

30 a. Definition of the net TOA and SFC energy fluxes

31 To quantify the excess (or deficit) of energy being absorbed by the atmosphere at any latitude,
32 we calculate the net downward flux of energy at the top of the atmosphere TOA and net downward
33 flux of energy at the surface SFC , and define their difference F_{net} as the atmospheric column
34 energy source:

$$TOA = SW_{TOA}^{\downarrow} - SW_{TOA}^{\uparrow} - LW_{TOA}^{\uparrow} \quad (1)$$

$$SFC = SW_{SFC}^{\downarrow} - SW_{SFC}^{\uparrow} + LW_{SFC}^{\downarrow} - LW_{SFC}^{\uparrow} - SH_{SFC} - LH_{SFC} \quad (2)$$

$$F_{net} = TOA - SFC \quad (3)$$

35 In equations 1-3, SW , LW , SH , and LH indicate shortwave radiation, longwave radiation, sensible
36 heat, and latent heat, respectively. The sign convention is such that a positive TOA represents
37 energy gained by the atmosphere plus ocean/land, while a positive SFC represents energy gained
38 by the surface. Positive values of F_{net} represent a gain of energy by the atmospheric column, either
39 from the TOA or the surface.

40 b. Cross-equatorial energy transport

41 Figure 10 of the main text shows a scatterplot of the location of the ITCZ, defined as the location
42 of the center of mass of precipitation between 30°S and 30°N, and the total atmospheric equatorial
43 energy transport $\langle vh \rangle$ at the equator $\phi = 0$:

$$\langle vh \rangle_0 = \frac{1}{g} \int_0^{2\pi} \int_{sfc}^{toa} v \times (c_p T + Lq + gz) \, d\lambda \, dp \quad (4)$$

44 In Eq. 4, $h = c_p T + L_v q + gz$ is the moist static energy, v is the meridional wind, T is the tempera-
45 ture of the air, q is water vapor mixing ratio, z is the height, c_p is the heat capacity for dry air, L is

46 the latent heat of vaporization, and g is the acceleration due to gravity. In the annual mean, cross-
47 equatorial atmospheric energy transport can be diagnosed from the hemispheric asymmetry in F_{net}
48 (Kang et al. 2008; Yoshimori and Broccoli 2008; Fasullo and Trenberth 2008; Donohoe et al.
49 2013). However, because atmospheric heat storage on sub-annual timescales is non-negligible,
50 we calculate cross-equatorial atmospheric heat transport from the column-integrated meridional
51 transport of moist static energy, both seasonally and in the annual mean in our simulations.

52 *c. Relationship between hemispheric energy balance and the latitude of the ITCZ*

53 The relationship between ITCZ location and cross equatorial energy transport shown in figures
54 10 and S7 is based on several assumptions that stem from physical arguments/constraints. These
55 are: (i) the overwhelming majority of energy transport is accomplished by the Hadley circulation
56 (Hadley 1735; Pierrehumbert 2002); (ii) the ITCZ is nearly co-located with the rising branch of
57 the Hadley circulation (Dima and Wallace 2003; Bischoff and Schneider 2014); (iii) the efficiency
58 of energy transport by the Hadley circulation is invariant to the climate state (i.e., the gross moist
59 stability is constant; see Neelin and Held (1987); Frierson (2007)); (iv) the ITCZ is nearly co-
60 located with with the position of the Energy Flux Equator (EFE, Kang et al. (2008); Bischoff and
61 Schneider (2014); see below); (v) the cross equatorial energy flux is linearly related to the distance
62 off the equator of the EFE (Bischoff and Schneider 2016); and (vi) that the energy tendency in the
63 atmosphere is small compared to the changes in the net energy F_{net} so that the system is nearly in
64 equilibrium.

65 These assumptions hold for annual averaged observations and annual average output from cli-
66 mate models run using various boundary conditions, including idealized aquaplanet simulations.
67 We point the reader to Geen et al. (2020) for a review of the theory and the evidence in support of
68 each of these assumptions. Here we only report the degree to which these assumptions hold in our

69 experiments. An alternative approach proposed by Privé and Plumb (2007) relates the location of
70 the ITCZ to the maximum of near-surface moist static energy rather than to inter-hemispheric en-
71 ergy imbalances (Bordoni and Schneider 2008), but in this work we focus primarily on the effect
72 of land heat capacity on inter-hemispheric energy imbalances.

73 Not surprisingly, the tropical energy transport in our various continental configurations is over-
74 whelmingly due to the Hadley circulation, and the ITCZ is nearly co-located with the rising branch
75 of the Hadley circulation (assumptions (i) and (ii) respectively; not shown). The tendency in at-
76 mospheric energy is generally very small compared to the changes in F_{net} (assumption (vi)).

77 The EFE is the latitude ϕ where the meridional energy transport $\langle vh \rangle$ is zero. Figure S7b shows
78 the cross equatorial energy flux is linearly related to the location of the EFE (assumption (v),
79 except for some distortion at the solstices in the Northland experiments. Figure S7c shows that
80 in our experiments, the EFE is a fair indicator of the position of the ITCZ (assumption (iv)) in
81 almost all seasons in both the Northland and Aqua experiments; the exception is for summertime
82 in the Northland experiments, when the Hadley circulation is somewhat distorted and there are
83 large changes in gross moist stability, violating assumption (iii). Finally, because the ITCZ is
84 nearly linearly related to the EFE latitude, and the cross equatorial energy transport $\langle vh \rangle_0$ is nearly
85 linearly related to the EFE, the ITCZ should also be linearly related to $\langle vh \rangle$. Figure S7a shows this
86 is roughly true, excepting the summer months in the Northland experiments where the location of
87 the EFE is distorted from the location of the ITCZ.

88 **References**

89 Bischoff, T., and T. Schneider, 2014: Energetic constraints on the position of the Intertropical
90 Convergence Zone. *Journal of Climate*, **27** (13), 4937–4951, doi:10.1175/JCLI-D-13-00650.1.

- 91 Bischoff, T., and T. Schneider, 2016: The equatorial energy balance, ITCZ position, and double-
92 ITCZ bifurcations. *Journal of Climate*, **29** (8), 2997–3013, doi:10.1175/JCLI-D-15-0328.1.
- 93 Bordoni, S., and T. Schneider, 2008: Monsoons as eddy-mediated regime transitions of the tropical
94 overturning circulation. *Nature Geoscience*, **1** (8), 515–519, doi:10.1038/ngeo248.
- 95 Dima, I. M., and J. M. Wallace, 2003: On the seasonality of the Hadley Cell. *Journal of the*
96 *Atmospheric Sciences*, **60** (12), 1522–1527, doi:10.1175/1520-0469(2003)060<1522:OTSOTH>
97 2.0.CO;2.
- 98 Donohoe, A., J. Marshall, D. Ferreira, and D. Mcgee, 2013: The relationship between ITCZ
99 location and cross-equatorial atmospheric heat transport: From the seasonal cycle to the Last
100 Glacial Maximum. *Journal of Climate*, **26** (11), 3597–3618, doi:10.1175/JCLI-D-12-00467.1.
- 101 Fasullo, J. T., and K. E. Trenberth, 2008: The Annual Cycle of the Energy Budget. Part II:
102 Meridional Structures and Poleward Transports. *Journal of Climate*, **21** (10), 2313–2325, doi:
103 10.1175/2007JCLI1936.1.
- 104 Frierson, D. M., 2007: The dynamics of idealized convection schemes and their effect on the
105 zonally averaged tropical circulation. *Journal of the Atmospheric Sciences*, **64** (6), 1959–1974,
106 doi:10.1175/JAS3935.1.
- 107 Geen, R., S. Bordoni, D. S. Battisti, and K. Hui, 2020: Monsoons, ITCZs and the Concept of the
108 Global Monsoon. *Reviews of Geophysics*, 1–45, doi:10.1029/2020rg000700.
- 109 Hadley, G., 1735: Concerning the Cause of the General Trade-Winds. *Royal Society of London*
110 *Philosophical Transactions Series I*, **39**, 58–62.

- 111 Kang, S. M., I. M. Held, D. M. W. Frierson, and M. Zhao, 2008: The Response of the ITCZ
112 to Extratropical Thermal Forcing: Idealized Slab-Ocean Experiments with a GCM. *Journal of*
113 *Climate*, **21** (14), 3521–3532, doi:10.1175/2007JCLI2146.1.
- 114 Neelin, J. D., and I. M. Held, 1987: Modeling tropical convergence based on the moist static
115 energy budget. 3–12 pp., doi:10.1175/1520-0493(1987)115<0003:MTCBOT>2.0.CO;2.
- 116 Pierrehumbert, R. T., 2002: The hydrologic cycle in deep-time climate problems. *Nature*,
117 **419** (6903), 191–198, doi:10.1038/nature01088.
- 118 Privé, N. C., and A. R. Plumb, 2007: Monsoon dynamics with interactive forcing. Part I: Axisym-
119 metric studies. *Journal of the Atmospheric Sciences*, **64** (5), 1417–1430, doi:10.1175/JAS3916.
120 1.
- 121 Yoshimori, M., and A. J. Broccoli, 2008: Equilibrium Response of an Atmosphere-Mixed Layer
122 Ocean Model to Different Radiative Forcing Agents: Global and Zonal Mean Response. *Journal*
123 *of Climate*, **21** (17), 4399–4423, doi:10.1175/2008JCLI2172.1.

124 **LIST OF TABLES**

125 **Table S1.** Average ($\pm 1\sigma$) area-weighted surface temperature for the whole globe, only
126 land areas, and only ocean areas for the annual mean, DJF, and JJA. Tem-
127 peratures and standard deviations are rounded to the nearest 0.1 K (i.e. ± 0.0
128 indicates interannual $\sigma < 0.1$ K). 9

129 **Table S2.** Table showing the hemispheric sum of the *SFC*, *TOA*, and *F_{net}* energy in PW
130 for the SH (left), NH (center), and the hemispheric imbalance (NH-SH, right),
131 rounded to the nearest 0.01 PW ($\pm 1\sigma$). Values correspond to integrating under
132 the black (*F_{net}*), blue (*TOA*), and green (*SFC*) curves over each hemisphere in
133 figure 12 of the main text. Positive ΔF_{net} implies energy transport from the NH
134 to the SH. 10

		Area-weighted Surface Temperature [K]					
		NorthlandBright			NorthlandDry		
		global	land	ocean	global	land	ocean
ANN		278.5 ± 0.1	277.1 ± 0.1	279.8 ± 0.0	275.3 ± 0.1	272.2 ± 0.2	278.4 ± 0.0
DJF		270.6 ± 0.1	259.3 ± 0.1	282.0 ± 0.1	267.6 ± 0.1	254.9 ± 0.2	280.3 ± 0.1
JJA		285.7 ± 0.1	293.6 ± 0.1	277.9 ± 0.0	282.4 ± 0.1	288.2 ± 0.2	276.6 ± 0.0
		NorthlandDark			Aqua		
		global	land	ocean	global	land	ocean
ANN		283.4 ± 0.0	284.5 ± 0.1	282.2 ± 0.0	284.6 ± 0.0	–	284.6 ± 0.2
DJF		275.5 ± 0.1	266.6 ± 0.1	284.5 ± 0.0	284.6 ± 0.0	–	284.6 ± 0.2
JJA		290.4 ± 0.0	300.7 ± 0.1	280.1 ± 0.0	284.6 ± 0.0	–	284.6 ± 0.3
		NorthWestLand			NorthWestLandDry		
		global	land	ocean	global	land	ocean
ANN		281.7 ± 0.1	281.7 ± 0.2	281.7 ± 0.0	281.3 ± 0.0	282.4 ± 0.2	280.9 ± 0.0
DJF		278.8 ± 0.1	268.1 ± 0.3	282.3 ± 0.1	278.1 ± 0.1	267.3 ± 0.3	281.6 ± 0.1
JJA		284.4 ± 0.1	294.4 ± 0.2	281.1 ± 0.0	284.4 ± 0.1	297.0 ± 0.2	280.4 ± 0.0
		PatchyLand			PatchyLandDry		
		global	land	ocean	global	land	ocean
ANN		281.7 ± 0.0	281.7 ± 0.1	281.6 ± 0.0	281.4 ± 0.0	282.7 ± 0.1	281.0 ± 0.0
DJF		279.1 ± 0.0	269.2 ± 0.2	282.2 ± 0.0	278.6 ± 0.0	269.1 ± 0.0	281.6 ± 0.0
JJA		284.1 ± 0.0	293.3 ± 0.1	281.2 ± 0.0	284.2 ± 0.0	295.6 ± 0.2	280.5 ± 0.0

135 TABLE S1. Average ($\pm 1\sigma$) area-weighted surface temperature for the whole globe, only land areas, and only
136 ocean areas for the annual mean, DJF, and JJA. Temperatures and standard deviations are rounded to the nearest
137 0.1 K (i.e. ± 0.0 indicates interannual $\sigma < 0.1$ K).

	SH			NH			Hemispheric Imbalance (NH - SH)		
	SFC [PW]	TOA [PW]	F_{net} [PW]	SFC [PW]	TOA [PW]	F_{net} [PW]	Δ SFC [PW]	Δ TOA [PW]	ΔF_{net} [PW]
ANN									
NLBright	0.07 ± 0.03	2.37 ± 0.03	2.44 ± 0.03	0.09 ± 0.01	-2.26 ± 0.04	-2.16 ± 0.03	0.03 ± 0.03	-4.63 ± 0.05	-4.61 ± 0.06
NLDark	0.06 ± 0.02	0.71 ± 0.04	0.77 ± 0.04	0.10 ± 0.02	-0.58 ± 0.04	-0.47 ± 0.04	0.05 ± 0.02	-1.29 ± 0.08	-1.24 ± 0.07
NLDry	0.06 ± 0.04	3.59 ± 0.02	3.65 ± 0.03	0.11 ± 0.03	-3.49 ± 0.05	-3.38 ± 0.03	0.05 ± 0.05	-7.08 ± 0.06	-7.03 ± 0.06
Aqua	0.03 ± 0.06	0.07 ± 0.03	0.10 ± 0.06	0.02 ± 0.02	0.07 ± 0.04	0.09 ± 0.05	-0.01 ± 0.07	0.00 ± 0.06	-0.01 ± 0.11
DJF									
NLBright	-15.18 ± 0.15	24.83 ± 0.04	9.65 ± 0.16	4.62 ± 0.12	-15.21 ± 0.07	-10.5 ± 0.14	19.80 ± 0.25	-40.04 ± 0.09	-20.24 ± 0.30
NLDark	-16.56 ± 0.16	23.50 ± 0.03	6.95 ± 0.17	5.28 ± 0.12	-15.27 ± 0.07	-9.99 ± 0.16	21.84 ± 0.24	-38.78 ± 0.08	-16.94 ± 0.31
NLDry	-14.62 ± 0.12	25.57 ± 0.03	10.95 ± 0.12	4.32 ± 0.08	-14.36 ± 0.07	-10.0 ± 0.08	18.94 ± 0.15	-39.93 ± 0.09	-20.99 ± 0.17
Aqua	-19.39 ± 0.08	22.31 ± 0.05	2.92 ± 0.09	19.04 ± 0.13	-21.86 ± 0.04	-2.82 ± 0.13	38.43 ± 0.15	-44.17 ± 0.08	-5.74 ± 0.16
MAM									
NLBright	7.77 ± 0.14	-4.86 ± 0.03	2.90 ± 0.15	-7.42 ± 0.15	5.93 ± 0.09	-1.49 ± 0.13	-15.18 ± 0.28	10.79 ± 0.11	-4.39 ± 0.25
NLDark	8.33 ± 0.12	-5.99 ± 0.04	2.34 ± 0.12	-7.84 ± 0.09	7.91 ± 0.12	0.07 ± 0.14	-16.17 ± 0.20	13.90 ± 0.15	-2.27 ± 0.24
NLDry	7.10 ± 0.12	-4.22 ± 0.02	2.88 ± 0.12	-7.27 ± 0.09	5.65 ± 0.08	-1.63 ± 0.15	-14.38 ± 0.20	9.87 ± 0.09	-4.51 ± 0.25
Aqua	7.77 ± 0.09	-7.45 ± 0.03	0.32 ± 0.08	-7.35 ± 0.12	7.30 ± 0.08	-0.05 ± 0.13	-15.12 ± 0.17	14.75 ± 0.08	-0.37 ± 0.18
JJA									
NLBright	17.00 ± 0.08	-19.61 ± 0.05	-2.61 ± 0.11	-3.52 ± 0.05	11.51 ± 0.12	7.99 ± 0.13	-20.52 ± 0.11	31.12 ± 0.16	10.60 ± 0.23
NLDark	17.65 ± 0.08	-21.68 ± 0.07	-4.03 ± 0.09	-3.31 ± 0.05	15.68 ± 0.11	12.37 ± 0.13	-20.96 ± 0.11	37.36 ± 0.16	16.40 ± 0.21
NLDry	16.75 ± 0.03	-18.32 ± 0.02	-1.57 ± 0.05	-3.24 ± 0.08	5.85 ± 0.19	2.61 ± 0.13	-19.99 ± 0.08	24.16 ± 0.21	4.18 ± 0.17
Aqua	19.10 ± 0.11	-21.86 ± 0.05	-2.76 ± 0.13	-19.4 ± 0.08	22.30 ± 0.06	2.90 ± 0.10	-38.50 ± 0.15	44.16 ± 0.10	5.66 ± 0.21
SON									
NLBright	-9.32 ± 0.08	9.14 ± 0.04	-0.18 ± 0.07	6.70 ± 0.04	-11.27 ± 0.05	-4.57 ± 0.05	16.02 ± 0.08	-20.41 ± 0.07	-4.39 ± 0.09
NLDark	-9.20 ± 0.11	7.01 ± 0.08	-2.20 ± 0.11	6.28 ± 0.06	-10.62 ± 0.04	-4.34 ± 0.07	15.48 ± 0.14	-17.63 ± 0.10	-2.14 ± 0.13
NLDry	-9.01 ± 0.08	11.34 ± 0.03	2.33 ± 0.10	6.61 ± 0.05	-11.09 ± 0.06	-4.47 ± 0.04	15.62 ± 0.11	-22.42 ± 0.04	-6.80 ± 0.11
Aqua	-7.35 ± 0.12	7.29 ± 0.06	-0.07 ± 0.11	7.80 ± 0.11	-7.45 ± 0.03	0.35 ± 0.11	15.15 ± 0.20	-14.74 ± 0.06	0.41 ± 0.20

138 TABLE S2. Table showing the hemispheric sum of the SFC , TOA , and F_{net} energy in PW for the SH (left),
139 NH (center), and the hemispheric imbalance (NH-SH, right), rounded to the nearest 0.01 PW ($\pm 1\sigma$). Values
140 correspond to integrating under the black (F_{net}), blue (TOA), and green (SFC) curves over each hemisphere in
141 figure 12 of the main text. Positive ΔF_{net} implies energy transport from the NH to the SH.

142 **LIST OF FIGURES**

143 **Fig. S1.** Spin-up of global mean surface temperatures. The values in the legend show the drift in
 144 temperature over the “spun-up” period, are calculated from a linear fit based on years 5
 145 (vertical black dashed line) to 50. 12

146 **Fig. S2.** Change in the zonal mean surface energy budget for NorthlandDark - NorthlandBright over
 147 the course of the year. The change in downwards LW is shown in (a) while the change in net
 148 SFC SW is shown in (b). LW emitted by the surface is shown in (c), while (d) and (e) show
 149 sensible and latent heat, respectively. (f) shows the change in net surface energy uptake
 150 ($E_{in} = SW^{\downarrow} - SW^{\uparrow} + LW^{\downarrow}$), where positive values indicate more energy into the surface; in
 151 the annual mean this would be balanced by $E_{out} = LW^{\uparrow} + LH + SH$ 13

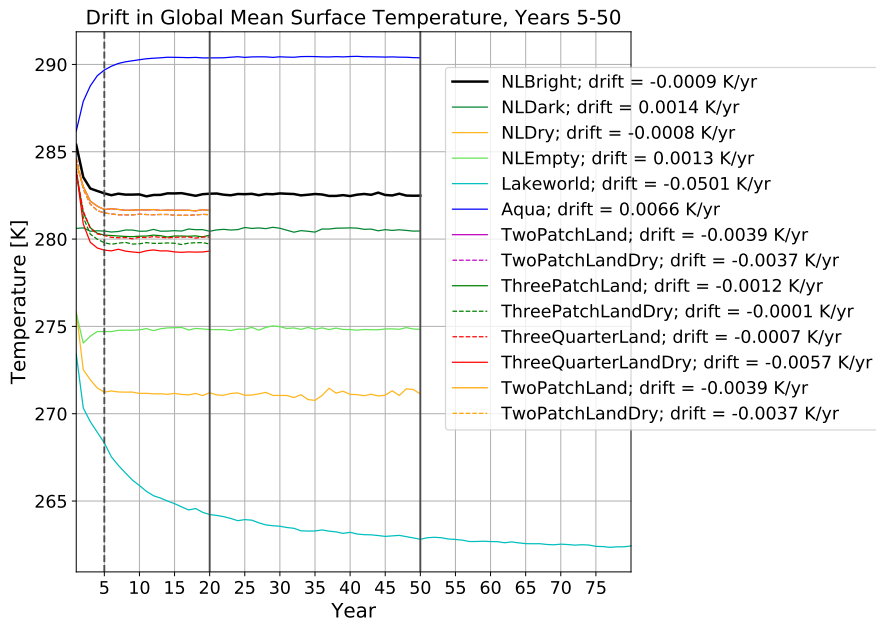
152 **Fig. S3.** Meridional streamfunction for DJF (left) and JJA (right) for NorthlandBright (a,b), North-
 153 landDark (c,d), NorthlandDry (e,f), and Aqua (g,h). Contours are spaced at 50×10^9 kg/s.
 154 14

155 **Fig. S4.** Cross-section of the zonal mean, annually averaged specific humidity [g/kg] for years 5-50
 156 of the Lakeworld simulation. The atmosphere is very dry except near the surface over the
 157 poles, but the peak specific humidity only reaches 1.75g/kg. The specific humidity is near-
 158 zero during the polar winter in each hemisphere (not shown). Note that the simulation does
 159 not reach equilibrium (see figure S1). 15

160 **Fig. S5.** Zonal mean surface temperature for the Lakeworld simulation. Annual mean tempera-
 161 tures are shown in black, June-July-August temperatures are shown in red, and December-
 162 January-February temperatures are shown in blue. Shading shows $\pm 1\sigma$ about the mean of
 163 years 5-50. The dashed grey line at 273.15 K shows the freezing temperature of water. Note
 164 that Lakeworld is actually cooling over this time period (see figure S1). 16

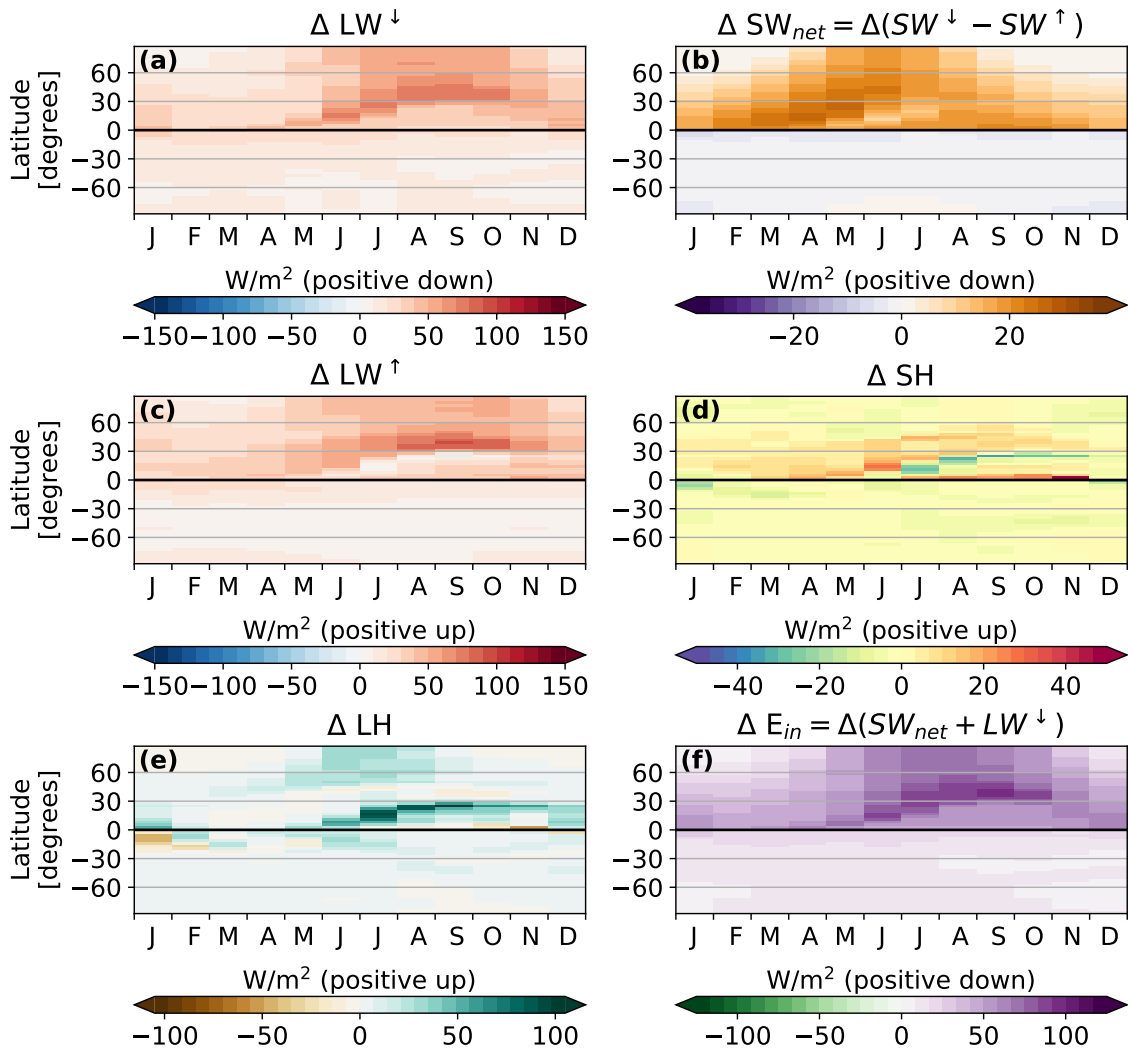
165 **Fig. S6.** Figure showing the “leak” of water from the all-land ISCA configuration. Global mean
 166 precipitation minus evaporation in mm/day (a,b), integrated terrestrial water storage in kg
 167 (c,d), and integrated atmospheric water content in kg (e,f) for Lakeworld (a,c,d) and North-
 168 landBright (b,d,f). Note the different y-axis ranges for the Lakeworld and NorthlandBright
 169 subplots. 17

170 **Fig. S7.** Relationship between (a) the latitude of the ITCZ and the magnitude of cross-equatorial en-
 171 ergy flux, (b) the latitude of the EFE and the magnitude of cross-equatorial energy flux, and
 172 (c) the latitude of the EFE and the latitude of the ITCZ. The latitude of the ITCZ is calcu-
 173 lated as the center of mass of precipitation between 30°S and 30°N; the latitude of the EFE
 174 is calculated as the zonal mean latitude where the vertical integral of polewards atmospheric
 175 energy transport $\langle v \cdot h \rangle = 0$; the magnitude of cross-equatorial energy flux is calculated as
 176 the magnitude of polewards atmospheric energy transport at the equator ($\langle v \cdot h \rangle_0$). Black
 177 markers indicate annual mean values, while blue, purple, green, and red markers indicate
 178 DJF, MAM, JJA, and SON averages, respectively. Circles show values for NorthlandBright,
 179 x for NorthlandDark, and triangles for Aqua. Each individual marker shows the seasonally
 180 averaged value for a single year of the time series. NorthlandDry is not included in the
 181 regression calculations here as the ITCZ effectively collapses over the continent. 18

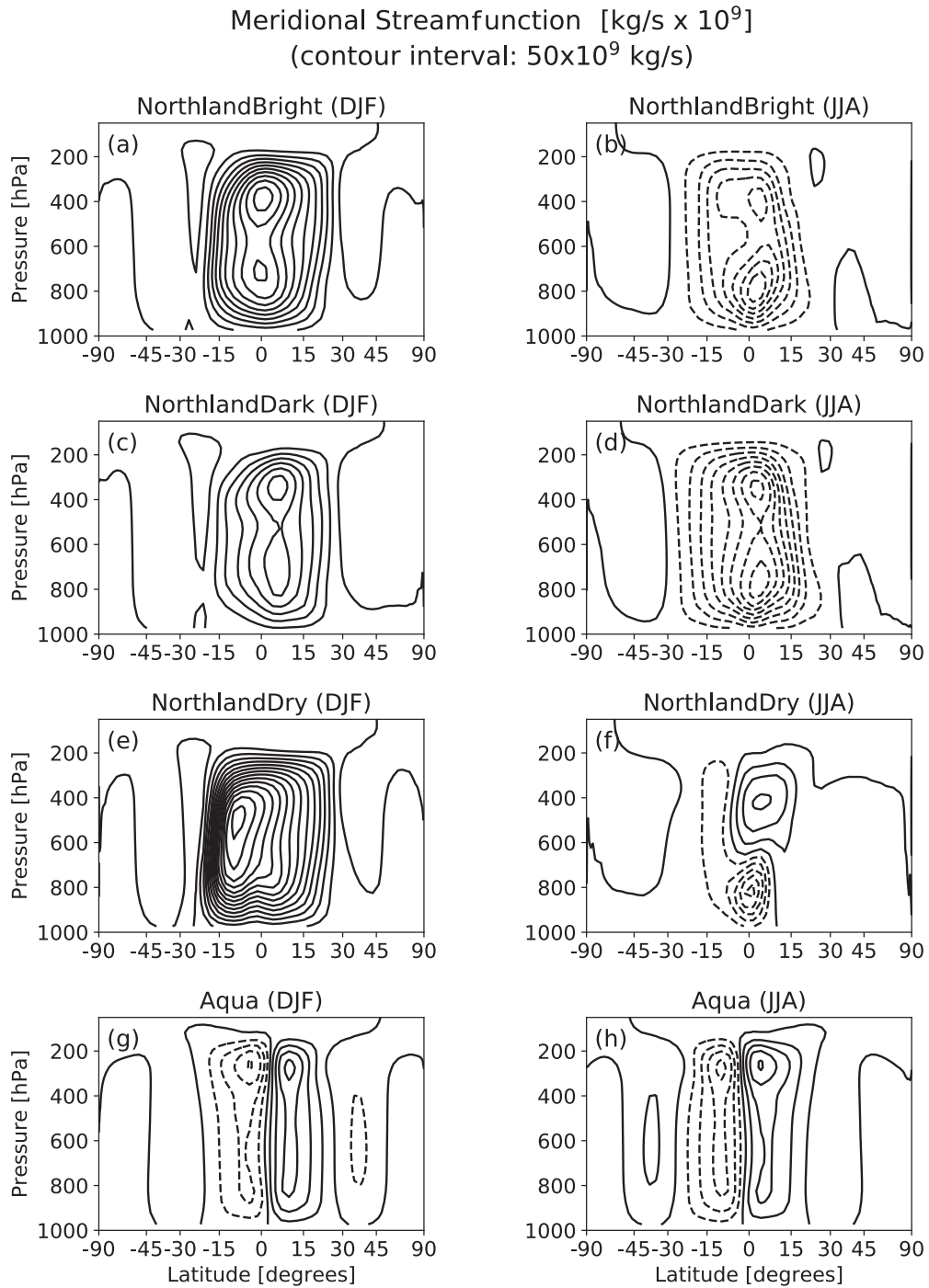


182 FIG. S1. Spin-up of global mean surface temperatures. The values in the legend show the drift in temperature
 183 over the “spin-up” period, are calculated from a linear fit based on years 5 (vertical black dashed line) to 50.

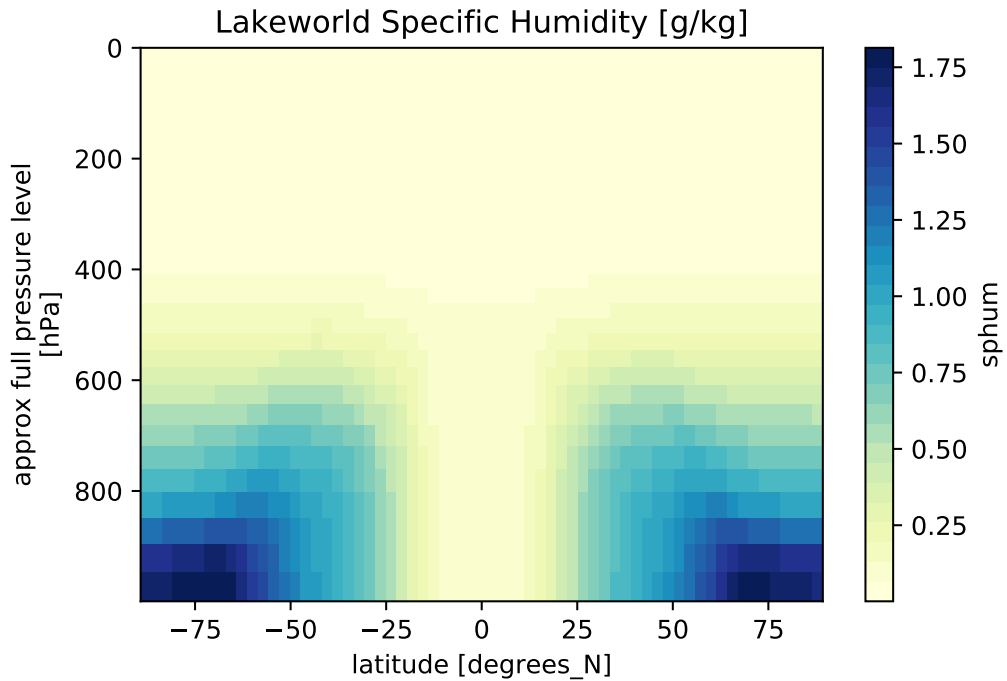
Δ SFC Energy Budget
NorthlandDark - NorthlandBright



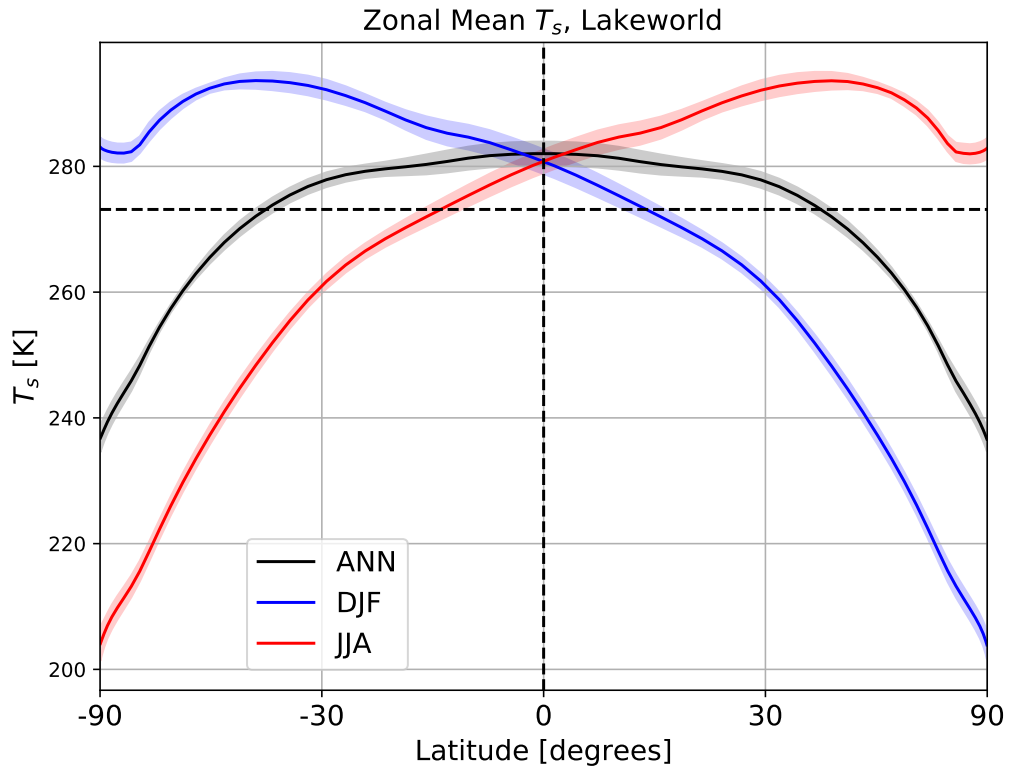
184 FIG. S2. Change in the zonal mean surface energy budget for NorthlandDark - NorthlandBright over the
 185 course of the year. The change in downwards LW is shown in (a) while the change in net SFC SW is shown in
 186 (b). LW emitted by the surface is shown in (c), while (d) and (e) show sensible and latent heat, respectively. (f)
 187 shows the change in net surface energy uptake ($E_{in} = SW^\downarrow - SW^\uparrow + LW^\downarrow$), where positive values indicate more
 188 energy into the surface; in the annual mean this would be balanced by $E_{out} = LW^\uparrow + LH + SH$.



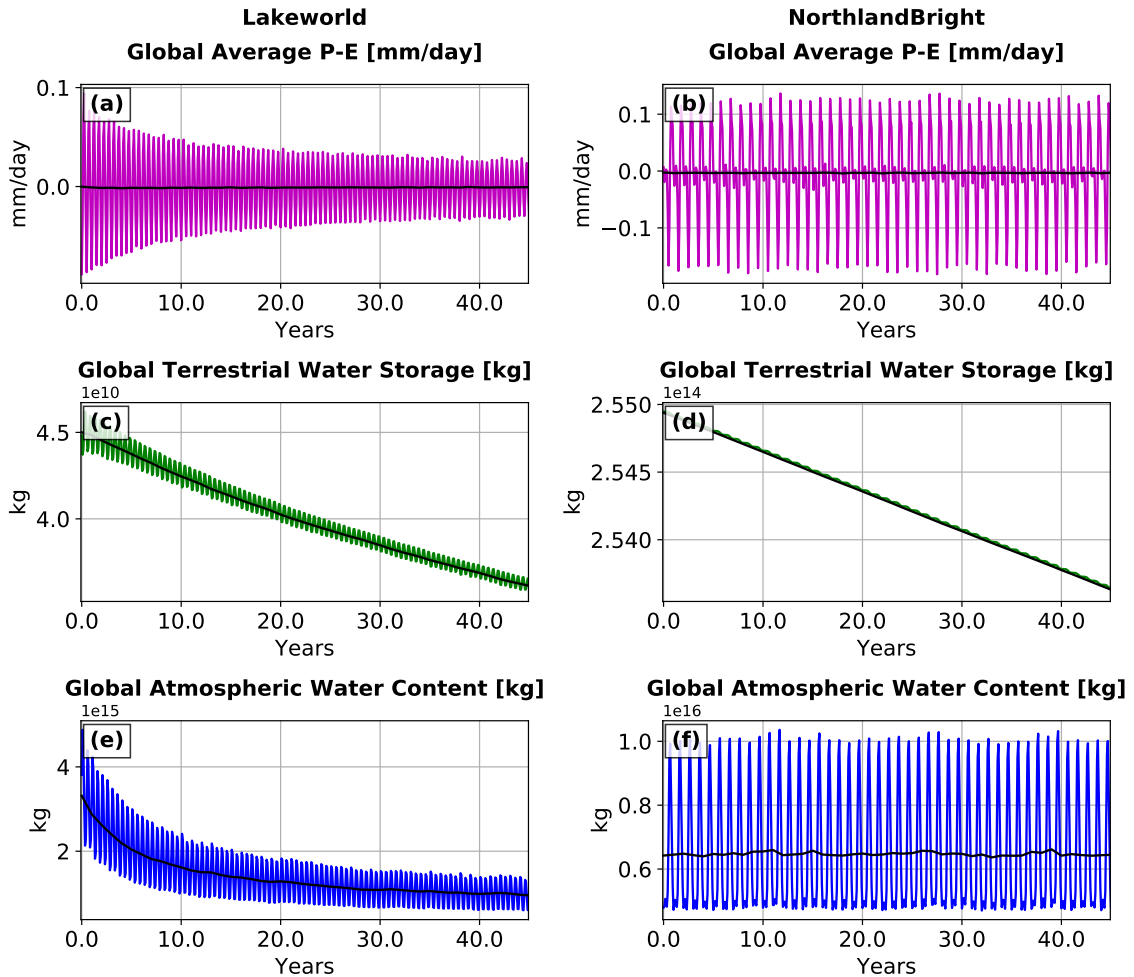
189 FIG. S3. Meridional streamfunction for DJF (left) and JJA (right) for NorthlandBright (a,b), NorthlandDark
190 (c,d), NorthlandDry (e,f), and Aqua (g,h). Contours are spaced at $50 \times 10^9 \text{ kg/s}$.



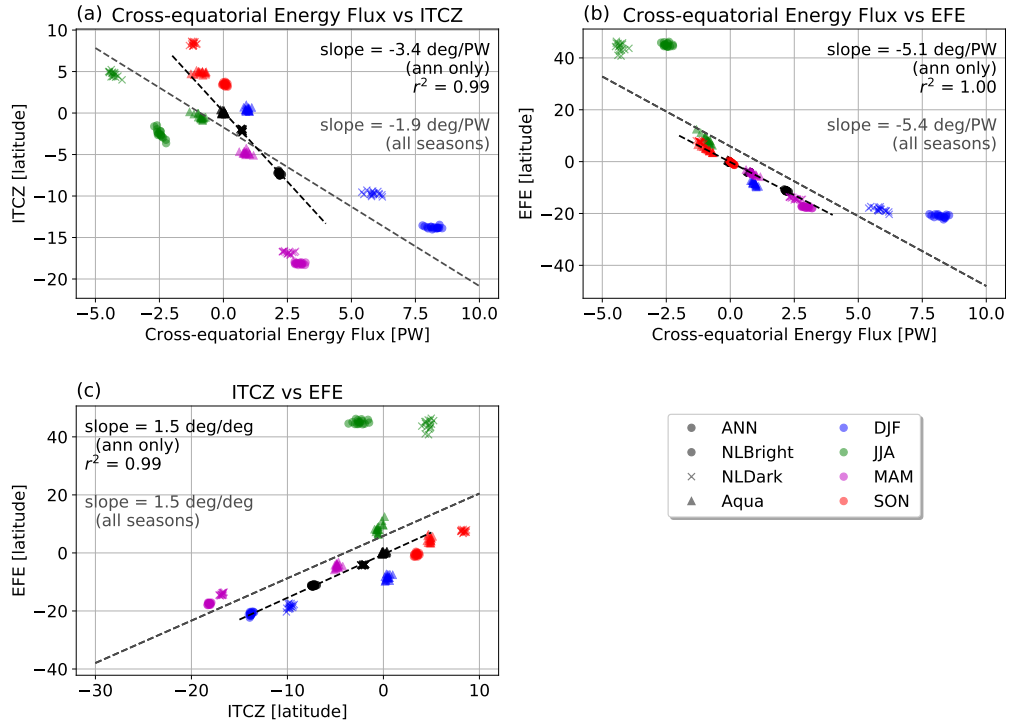
191 FIG. S4. Cross-section of the zonal mean, annually averaged specific humidity [g/kg] for years 5-50 of the
 192 Lakeworld simulation. The atmosphere is very dry except near the surface over the poles, but the peak specific
 193 humidity only reaches 1.75g/kg. The specific humidity is near-zero during the polar winter in each hemisphere
 194 (not shown). Note that the simulation does not reach equilibrium (see figure S1).



195 FIG. S5. Zonal mean surface temperature for the Lakeworld simulation. Annual mean temperatures are shown
 196 in black, June-July-August temperatures are shown in red, and December-January-February temperatures are
 197 shown in blue. Shading shows $\pm 1\sigma$ about the mean of years 5-50. The dashed grey line at 273.15 K shows the
 198 freezing temperature of water. Note that Lakeworld is actually cooling over this time period (see figure S1).



199 FIG. S6. Figure showing the “leak” of water from the all-land ISCA configuration. Global mean precipitation
 200 minus evaporation in mm/day (a,b), integrated terrestrial water storage in kg (c,d), and integrated atmospheric
 201 water content in kg (e,f) for Lakeworld (a,c,d) and NorthlandBright (b,d,f). Note the different y-axis ranges for
 202 the Lakeworld and NorthlandBright subplots.



203 FIG. S7. Relationship between (a) the latitude of the ITCZ and the magnitude of cross-equatorial energy
 204 flux, (b) the latitude of the EFE and the magnitude of cross-equatorial energy flux, and (c) the latitude of the
 205 EFE and the latitude of the ITCZ. The latitude of the ITCZ is calculated as the center of mass of precipitation
 206 between 30°S and 30°N; the latitude of the EFE is calculated as the zonal mean latitude where the vertical
 207 integral of polewards atmospheric energy transport $\langle v \cdot h \rangle = 0$; the magnitude of cross-equatorial energy flux is
 208 calculated as the magnitude of polewards atmospheric energy transport at the equator ($\langle v \cdot h \rangle_0$). Black markers
 209 indicate annual mean values, while blue, purple, green, and red markers indicate DJF, MAM, JJA, and SON
 210 averages, respectively. Circles show values for NorthlandBright, x for NorthlandDark, and triangles for Aqua.
 211 Each individual marker shows the seasonally averaged value for a single year of the time series. NorthlandDry
 212 is not included in the regression calculations here as the ITCZ effectively collapses over the continent.